SAN-based block polymers as a platform for manufacturing strong isoporous membranes

Adam N. Mann, Noah P. Wamble, Louise Kuehster, Matthew R. Landsman, Anthony J. Arrowood, Gregory M. Su, Nathaniel A. Lynd, Benny D. Freeman, and Gabriel E. Sanoja*

For Table of Contents use only

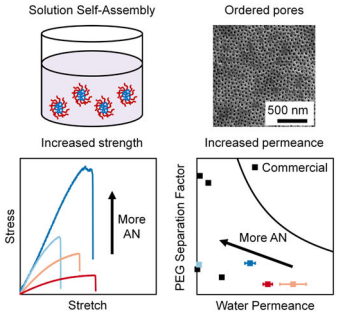

Abstract

Ultrafiltration (UF) membranes are ubiquitous in water purification and bioprocessing. However, co-designing their mechanical and transport properties remains challenging because of the broad pore size distributions at the surface and within the bulk that result from nonsolvent-induced phase separation (NIPS) – their typical manufacturing process. These distributions influence the hydrodynamic resistance to water flow and the stress concentrations around the pores. Developing advanced UF membranes requires innovative molecular designs that offer control over the surface and bulk pores, as well as the mechanical properties of the load-bearing, polymer.

We introduce a platform for designing UF membranes by leveraging solution self-assembly of block polymers and chain architectures with pendant polar groups. The block polymers consist of a poly(styrene-*co*-acrylonitrile) hydrophobic block, which is known for its strength, and a poly(4-vinyl pyridine) hydrophilic block, which drives solution self-assembly. We focus on a series of block polymers with constant molecular weight, $M_n \approx 115$ kDa, SAN fraction, 75 wt.%, and varying acrylonitrile content, 0 to 40 mol%, to demonstrate that: (i) RAFT dispersion copolymerization of acrylonitrile and styrene provides a facile route to synthesize strong block polymers, (ii) incorporation of acrylonitrile into the hydrophobic block enhances membrane strength by facilitating chain entanglements and dipole-dipole interactions, and (iii) acrylonitrile alters the balance between membrane permeance and rejection, even when the membranes feature similar surface and bulk pores. Overall, our results provide insights into the molecular design of UF membranes with enhanced mechanical and separation properties, contributing to the development of materials for water and energy technologies.

Introduction

Nonsolvent-induced phase separation (NIPS) is the predominant method for manufacturing ultrafiltration (UF) membranes [1–6] because it is simple, scalable, and compatible with thermoplastic polymers, such as polysulfone (*e.g.*, Udel) and polyamide-imide (*e.g.*, Torlon) [7]. In practice, this process also requires polymers with excellent thermochemical stability and mechanical properties, since membranes commonly experience stresses, chemical treatments, and temperature fluctuations during operation and manufacturing. For instance, polysulfone – a state-of-the-art UF membrane - is thermally stable up to 450 ^{o}C, chemically stable at pH values from 2 to 13, and resistant to oxidative agents and certain hydrocarbon oils [8]. In addition, it exhibits outstanding mechanical properties, with a bulk tensile strength of σ_f = 70 MPa and a strain at break of ε_f ~ 25 - 100% [9], outperforming commodity glassy polymers such as polystyrene, which typically have σ_f = 40 MPa and ε_f=5% [10]. This combination of mechanical strength and ductility allows polysulfone membranes to sustain significant stresses during both manufacturing and operation while minimizing hydrodynamic resistance to water flow. As a result, polysulfone membranes are effective at stabilizing stress concentrations near pores, ensuring reliable performance in demanding environments [11].

Despite advancements in narrowing the size distribution of surface pores and improving rejection curves (*i.e.*, selectivity) [12–15], relatively few studies have examined the mechanical properties of UF membranes [16,17]. Many efforts have focused on developing “isoporous” membranes composed of block polymers, such as poly(styrene-*b*-4-vinyl pyridine) (S4VP), rather than homopolymers, which attain a uniform surface structure from solution self-assembly prior to NIPS [13,14]. However, in spite of their narrow pore size distributions, “isoporous” membranes typically

exhibit poor mechanical properties, with a tensile strength of $\sigma_f \approx 1$ MPa and a strain at break of $\varepsilon_f \approx 0.5\%$, meaning they are highly prone to fracture and unsuitable for scalable manufacturing [16]. This work aims to address this challenge by providing molecular-based rationale for co-designing mechanical and transport properties of "isoporous", block polymer membranes. By revisiting the mechanics of polymer glasses and applying these principles to the molecular engineering of block polymers, it introduces a membrane platform with improved mechanical properties and a similar permeance-rejection trade-off than conventional homopolymer-based membranes.

It recognizes the key molecular factors contributing to the fracture toughness of glassy polymers, defined here as the energy required to propagate a crack. For example, the entanglement chain density, which ultimately governs the failure mode [18–22]. Specifically, at low entanglement densities, fibrillated structures called crazes form [23–25], which rapidly coalesce into cracks and result in brittle-like fracture [26–28]. In contrast, at high entanglement densities, banded regions known as shear deformation zones (SDZs) evolve, which can lead to stable necking, yielding, and a ductile-like behavior [29–33]. Thus, entangled polymers are critical for manufacturing mechanically robust UF membranes.

Consider the relationship between polymerization mechanism, molecular weight, and entanglement density in common polymers, especially those used in UF. Ductile polymers, such as polycarbonate and polysulfone, typically result from step-growth polymerization and feature bulky aromatic groups along their backbones. These polymers pack effectively in space, resulting in low entanglement molecular weights (M_e) (*i.e.*, packing lengths), and excellent mechanical properties [34,35]. In contrast, brittle polymers like polystyrene are often derive from chain-growth polymerization and contain bulky aromatic groups along their side chains. These polymers arrange

inefficiently in space, leading to higher packing lengths, entanglement molecular weights, and excessive brittleness.

This examination of already-established structure-property relationships suggests that manufacturing mechanically robust "isoporous" membranes by NIPS requires block polymers with highly entangled structural (*i.e.*, hydrophobic) blocks. However, this condition presents a fundamental challenge in polymer science, as block polymers typically result from chain-growth rather than step-growth polymerization – with notable exceptions, such as poly(sulfone-*b*-ethylene glycol) [36,37].

One route to address this problem is to copolymerize styrene with a polar, less bulky comonomer, such as acrylonitrile (AN) [38]. Donald and Kramer illustrated this point by examining the mechanical properties of a series of poly(styrene-*co*-acrylonitrile) (SAN) statistical copolymers [39]. Specifically, they showed that at 24 mol% AN and M_n = 102 kDa, SAN copolymers are more ductile than polystyrene, forming a mixture of crazes and SDZs. Yet, at 66 mol% AN and $M_n \approx 56$ kDa, these copolymers only develop SDZs, indicating greater ductility despite lower M_n. Two factors likely contribute to this change in failure mode: (i) dipole-dipole interactions, and (ii) chain entanglements [10,40,41]. Thus, the work of Donald and Kramer highlights a pathway for designing block polymer membranes that combine high mechanical strength with narrow pore size distributions, addressing a key challenge in the development of advanced UF membranes.

In this work, we investigated the potential of AN to improve the mechanical properties of the most widely used block polymer in self-assembly assisted-NIPS (SNIPS): poly(styrene-*b*-4-vinyl pyridine) (S4VP). We hypothesized that incorporating AN into the polystyrene block of S4VP would increase the strength and toughness of the resulting membranes without compromising their separation performance. To test this hypothesis, we synthesized a series of poly[(styrene-*co*-

acrylonitrile)-*b*-(4-vinyl pyridine)] (SAN4VP) block polymers using RAFT dispersion polymerization, varying the AN content in the styrenic structural block. We then processed these block polymers into membranes via SNIPS, and characterized the structure, transport properties, and mechanical properties of the resulting membranes by Scanning Electron Microscopy (SEM), pure water permeance measurements, poly(ethylene glycol) (PEG) rejection experiments, and tensile, fragility, and fracture testing. Our results demonstrate that adding AN to S4VP block polymers yields membranes that are strong, permeable, and "isoporous", with higher permeance than conventional UF membranes despite their comparable separation performance.

Materials and Methods

Materials

All reagents were purchased from Millipore-Sigma and used as received unless specified otherwise, including 2,2′-azobis(2-methyl- propionitrile) (AIBN, 98%, stored at -15 °C), *sec*-butyllithium (1.4 M in cyclohexane), calcium hydride (Thermo Scientific, ca. 93%), di-*n*-butylmagnesium (1.0 M in heptane), ethylaluminum sesquichloride (Thermo Scientific, 0.4 M in hexane), 4-cyano-4-[(dodecylsulfanylthiocarbonyl)-sulfanyl] pentanoic acid (CDTPA, 97%, stored at 5 °C), ethanol (99.5%), methanol (99.8%), chloroform (99.8%), anhydrous 1,4-dioxane (DOX, 99.8%), anhydrous tetrahydrofuran (THF, 99.9%) and anhydrous N,N-dimethylformamide (DMF, 99.8%).

A Millipore Milli-Q Advantage A-10 system, fed with reverse osmosis (RO) water, was used to produce deionized (DI) water at approximately 23 ^{o}C and a resistivity of 18.2 MΩ·cm^{-1}. This water was then utilized as the nonsolvent (*i.e.*, coagulation medium) in the manufacturing of membranes by SNIPS.

Styrene (≥ 99.9%), acrylonitrile (99%), and 4-vinylpyridine (4VP, 97%) were purified by column chromatography, eluting through a basic aluminum oxide (> 98%) column to remove any free radical inhibitors. Tetrahydrofuran (unstabilized HPLC-grade, Spectrum Chemical) solvent was also purified by column chromatography, passing through two alumina columns mounted on a JC Meyer solvent purification system. Finally, dichloromethane (ACS grade) and methanol (ACS grade) were purchased from Fisher and used as received.

Commercial polyacrylonitrile (PAN; SKU: YMPX3001), polyethersulfone (PES-100, SKU: YMLX3001; PES-300, SKU: YMLY3001) – sourced from Synder Filtration (Vacaville, CA) – and polysulfone (PS-20; M-PS20-GPP) membranes – sourced from Nanostone Water (Eden Prairie, MN) – were used as references to evaluate separation performance.

Copper grids were kindly provided by Prof. Michael L. Chabinyc (UCSB).

Synthesis of S4VP block polymer by anionic polymerization

Tetrahydrofuran (THF, 500 mL) was degassed using three freeze-pump-thaw cycles and then distilled first over di-*n*-butylmagnesium and then over ethylaluminum sesquichloride into two burets fitted with Teflon valves. Subsequently, styrene (80 mL) was stirred over calcium hydride, and then distilled first over di-*n*-butylmagnesium and finally into a graduated buret with a Teflon valve. Finally, 4-Vinyl pyridine (18.4 mL, 172 mmol, 246 eq.) was distilled over calcium hydride into a buret equipped with a Teflon valve, and diluted with purified THF (*ca.* 100 mL) - distilled into the same buret. Styrene, 4-vinyl pyridine, and THF were stored in their burets at 2 °C for no longer than 12 h before use.

Each buret was attached to a custom 2 L reactor equipped with ACE-thread ports and a glass-coated magnetic stir bar. A glass vacuum line, sealed with a septum, was fitted to the reactor for connection to a Schlenk line using flexible stainless-steel tubes, and the remaining ports were

plugged with nylon stoppers. The reactor was fully evacuated to below 10 mTorr and refilled with nitrogen four times before being placed in an isopropanol bath on a magnetic stir plate. The reactor was then isolated from the vacuum line, and both THF burets were emptied into the reactor.

Styrene (59 mL, 513 mmol, 733 eq.) was added to the reactor using the graduated buret, and the reactor was backfilled with nitrogen. The bath was cooled to -78 °C using dry ice in isopropanol, and this temperature maintained to the best of our ability by continuously adding dry ice during the polymerization. The styrene/THF mixture was allowed to equilibrate at -78 ºC for 40 minutes before sec-butyllithium solution (0.5 mL, 0.7 mmol, 1 eq.) was introduced. Upon addition of sec-butyllithium, the solution turned bright orange. After 3 h, the buret containing 4VP was cooled by wrapping an aluminum foil funnel around it and filling the funnel with dry ice. After 40 min of cooling, the buret was opened slightly and 4VP was added dropwise into the reactor. The 4VP was allowed to react for 6 h, after which degassed methanol (2 mL) was added to terminate the polymerization.

The resulting polymer was partially dried, resuspended in dichloromethane, and precipitated into methanol. The precipitate was filtered from the methanol and dried under vacuum (5 mtorr), yielding a white solid powder. The molecular weights were M_n (NMR) = 85 kDa PS, 27 kDa P4VP; M_n (SEC, relative to PS standards) = 150 kDa, Đ = 1.47. ^{1}H NMR spectroscopy (400 MHz, CD_2Cl_2) revealed the following chemical shifts δ: 7.98-8.68 (m, 4VP (2H)), 6.09-7.50 (m, 4VP (2H) and styrene (5H)) (see spectrum in **Fig. S1**).

Synthesis of P4VP macromolecular chain transfer agent by RAFT polymerization

A P4VP macromolecular chain transfer agent was synthesized through RAFT polymerization. CDTPA (360.6 mg, 0.89 mmol, 1 eq.) and AIBN (91.2 mg, 0.56 mmol, 0.6 eq.) were dissolved in 4VP monomer (29.4 g, 280 mmol, 314.5 eq.), at an equivalent ratio of [4VP]/[CDTPA]/[AIBN] =

315:1:0.6. To this solution, ethanol (100 mL) was added. The pre-polymerization solution was degassed with four freeze-pump-thaw cycles and then filled with nitrogen gas. The polymerization was conducted in a 250 mL single neck, AirFree® round bottom flask (Chemglass Life Sciences) at 70 °C, stirring at 600 rpm for 24 h.

The reaction was quenched by cooling the mixture in a room--temperature water bath and exposing it to air. The crude polymer was precipitated twice from ethanol into *n*-hexane and dried overnight under vacuum at 40 °C. The resulting P4VP macromolecular RAFT agent was obtained as a pale reddish-orange powder. Monomer conversion, as calculated from ^{1}H NMR spectroscopy, was 88%, yielding M_n = 29 kDa. The ^{1}H NMR spectrum (400 MHz, $CDCl_3$) showed peaks at δ (ppm) = 8.30, 6.37 (m, 4H, Ph) (see **Fig. S2**).

Synthesis of SAN4VP block polymers through dispersion polymerization

To grow the second block of SAN4VP, the following procedure was typically employed: The P4VP macromolecular RAFT agent (2.88 g, 0.11 mmol, 1 eq.) was dissolved in 30 mL of an 80:20 (v/v) methanol/water mixture. AIBN (1.8 mg, 0.015 mmol, 0.13 eq.) was added as a solution in 700 μL of the same methanol/H_2O mixture. Then, styrene (10.91 g, 0.105 mol, 955 eq.) and acrylonitrile (0.98 g, 0.0185 mol, 168 eq.) were introduced, and the total solids content was adjusted to around 20 wt.% by adding an additional 32 mL of the methanol/H_2O mixture.

The pre-polymerization solution was degassed by four freeze-pump-thaw cycles and backfilled with nitrogen. The polymerization was conducted in a 250 mL single neck, AirFree® round bottom flask (Chemglass Life Sciences) at 70 °C, stirring at 850 rpm for 24 h. The reaction was terminated by cooling the flask in a room-temperature water bath and exposing the contents to air. The methanol/H_2O solvent blend was removed from the crude polymer by rotary evaporator.

To purify the polymer and remove any unreacted monomers and impurities, the crude polymer was dissolved in THF, precipitated twice into *n*-hexane, and then dried overnight under vacuum at 40 °C. The resulting dried polymer was obtained as a pale-yellow powder. The monomer conversion, as determined by ^{1}H NMR spectroscopy, was 95%. The ^{1}H NMR spectrum ($CDCl_3$) showed peaks at δ (ppm): 8.30, 6.37 (m, 4H, Ph), 7.07 (broad s, 5H, Ph) (see spectra in **Figs. S3-S5**, and GPC traces for all block polymers in **Fig. S6**).

Solvent casting of dense films

Dense block polymer films were cast by dissolving around 1.5 g of dry polymer in 30 g of chloroform. The polymer solution was stirred overnight to ensure complete dissolution. The solution was then filtered through a 0.45 μm PTFE syringe filter to remove particulates. The filtered solution was poured into a 9-cm diameter PTFE casting dish placed on a levelling plate located inside a vacuum oven.

To facilitate solvent evaporation, a compressed air flow rate of 20 ft^3(STP)/h was directed over the solution. The compressed air was passed through a desiccant to remove atmospheric moisture, and a funnel was positioned above the casting dish to control the evaporation rate. After casting, the film was gradually heated under vacuum to remove residual solvent, ramping to a final temperature of 150 °C over 48 h.

Thermogravimetric Analysis (TGA)

Thermogravimetric analysis was performed to determine degradation temperature (T_d) using a TA Instruments Q500 TGA. A dense film sample weighing 7.5-10 mg was placed on a platinum pan. Nitrogen was used as cooling gas and air as purge gas, both at a flow rate of 10 mL/min. The oven was heated from 25 to 500 °C at a rate of 5 °C/min (see thermograms for all block polymers in **Fig. S8**).

Differential Scanning Calorimetry (DSC)

DSC was performed to determine glass transition temperatures (T_g) using a TA Instruments DSC 2500. 5.4 mm diameter samples of dense polymer films were punch-cut to fit into aluminum pans. After sealing the pans, samples were heated and cooled between 20 to 200 ºC three times (see thermograms for all block polymers in **Fig. S9**).

Uniaxial tensile tests

Tensile tests were performed on an Instron 34TM5 equipped with a 100 N load cell. Dense films and hydrated, unsupported porous membranes were punch-cut into dog bone-shaped specimens of 20 mm gauge length and 4 mm width. The thickness of these specimens was measured three times along the gauge length using a micrometer to calculate the average thickness. The specimens were stretched at an initial rate of 0.003 s^{-1}, and the stress and stretch were estimated from the force-displacement data according to:

$$\sigma = \frac{F}{A_{cross}} = \frac{F}{tw} \tag{1}$$

and

$$\lambda = \frac{l}{l_0} \tag{2}$$

where σ is the nominal stress, F is the force, A_{cross} is the initial cross-sectional area, t is the initial specimen thickness, w is the specimen width, and l and l_0 are the deformed and undeformed specimen lengths, respectively.

Three replicates were tested for each membrane. From the stress-stretch curves, the elastic modulus, E, and the tensile strength (i.e., stress at break), σ_f, were calculated according to:

$$E = \left(\frac{d\sigma}{d\lambda}\right)|_{\lambda=1.005} \tag{3}$$

and

$$\sigma_f = max(\sigma) \tag{4}$$

Single-edge notch crack propagation

Dense films were punch-cut into dog-bone-shaped specimens of 20 mm gauge length, 4 mm width, and approximately 0.2 mm thickness. A fresh razor blade was used to introduce a crack approximately 1 mm in length. Specimens were deformed at a crosshead speed of 0.06 mm s^{-1} (i.e., initial stretch rate of 0.003 s^{-1}) using an Instron 34TM5 equipped with a 100 N load cell. The resulting force−displacement curves were used to compute nominal stress, σ, stretch, λ, and fracture toughness or critical stress intensity factor, K_c [42], according to:

$$K_c = Q\sigma_c a^{1/2} \tag{5}$$

where

$$Q = 1.99 - 0.41\left(\frac{a}{w}\right) + 18.70\left(\frac{a}{w}\right)^2 - 38.48\left(\frac{a}{w}\right)^3 + 53.85\left(\frac{a}{w}\right)^4 \tag{6}$$

Here, Q is a geometry parameter, σ_c is the applied stress at the onset of crack growth, a is the initial length of the sharp crack, and w is the specimen width (see representative stress-stretch curves of pre-notched specimens in **Fig. S11**).

Copper grid fragility test

The deformation mechanism of dense block polymer films was investigated using a copper grid fragility test [28,43]. This method allows simultaneous, independent, tensile deformation of numerous specimens, coated and adhered onto grid squares, providing information on the probability of craze nucleation and subsequent crack growth.

Thin polymer films were prepared by spin-coating a 4 wt.% solution in chloroform at 1000 RPM for 1 min onto clean glass substrates. After drying, the films were cut into approximately 25 × 10 mm rectangles using a razor blade and carefully floated off the glass onto a water bath. The floating films were then transferred onto pre-treated copper grids.

Prior to use, the copper grids were annealed at 650 ºC for 15 min under an argon atmosphere – a temperature identified by Kramer and co-workers in previous work [19,26,33,39,43] - to enhance ductility and promote uniform straining of the metal framework. After floating the block polymer film onto the grid, the assembly was exposed to chloroform vapor for 30 min in a sealed container. This vapor treatment step improves adhesion of the polymer film to the grid bars and removes interfacial wrinkles. Finally, the adhered films were dried overnight at 40 ºC under dynamic vacuum to eliminate residual solvent without altering the polymer mesostructure.

The deformation modes of the polymer films were analyzed using a custom-built strain frame mounted on an optical microscope. The copper grid was incrementally deformed to various strain levels, and the fraction of grid squares, p, exhibiting crazes, SDZs, and/or cracks was quantified at each strain.

Importantly, grid annealing, chloroform-vapor exposure, and vacuum drying were all considered essential for these fragility measurements. Two factors contributed to this consideration. First, annealing at lower temperatures could compromise copper ductility, causing metal failure before polymer crazing, shear banding, or fracture. Second, modifying the chloroform-vapor exposure time or drying conditions could alter the polymer mesostructure or dynamics via plasticization, thereby affecting the measured mechanical properties.

Grazing-incidence small-angle x-ray scattering (GI-SAXS) of block polymer solutions

To study the effect of AN on solution self-assembly, GI-SAXS profiles were acquired on blade-coated cast solutions. These experiments were performed at 16.1 keV using beamline 12-ID of NSLS-II during the membrane casting process. The experimental setup included an automated syringe pump (New Era Pump Systems, Inc., East Farmingdale, NY, USA) and a linear translation stage (Thorlabs, Newton, NJ, USA) positioned below the casting blade. The syringe pump and blade-coater were fully automated using the Bluesky/EPICS software platform [44].

During a typical GI-SAXS experiment, a pristine silicon wafer was secured on the stage using tape and the X-ray beam was aligned at an incidence angle of 0.12°. Then, a syringe pump dispensed 500 μL of block polymer solution onto the wafer, after which the translation stage moved beneath a casting blade set to a thickness of 200 μm, spreading the solution into a thin film. GI-SAXS profiles were captured using a Pilatus 1M detector positioned approximately 9 m downstream from the sample. Data collection began just before the casting process, allowing the initial time to be precisely determined by observing the beam reflection from the cast film in the detector images. GI-SAXS data were acquired for 5 minutes at a rate of 1 image per second to monitor the nonequilibrium phase separation processes during block polymer membrane formation. Horizontal linecuts from the GI-SAXS data, used to analyze the in-plane ordering of polymer structures on the membrane surface, were processed with the Python-based SMI-analysis package (see profiles in **Fig. S10**).

Non-solvent induced phase separation of block polymer solutions

Each casting solution was poured onto a cleaned glass plate, and a 4-inch Gardco doctor blade was used to meter the solution to a uniform thickness of 200 μm. The coating was applied using a Gardco Automatic Drawdown Machine II (DP-8301) at a velocity of approximately 23 cm/s (shear rate = 1,150 s^{-1}). The cast solution was then left to dry for 25 s in ambient air at roughly 23 ºC and 50 ± 5% relative humidity. After this drying step, the cast solution was immersed in a 23 ºC DI water bath to induce phase inversion and form a porous membrane. The resulting membranes were soaked in a beaker filled with DI water for 24 h to remove any residual solvent.

Scanning electron microscopy

Samples for scanning electron microscopy (SEM) were prepared by immersing the cast membranes in methanol for at least 1 min and air-drying them in ambient conditions. For top and

bottom surface imaging, membrane samples were mounted on SEM stems. Cross-sections were prepared by briefly soaking the membranes in methanol, freezing them in liquid nitrogen for at least 30 s, and fracturing them with flat tweezers. All samples were sputter-coated with a 40:60 Au/Pt alloy for 90 s at 40 mA and imaged using an Apreo 2C LoVac SEM operating at 20 kV with a spot size of 3.0 and a working distance of 10 mm (see representative SEM images in **Figs. S12-S16**).

Porosity quantification by image analysis

Cross-sectional SEM images of the cast membranes were processed using an image segmentation protocol introduced by Bridge *et al*. [45]. Briefly, the images were binarized (*i.e.*, thresholded), and the macroporosity or macrovoid areal fraction, D_m, was estimated according to:

$$D_m = \frac{N_0}{N_0+N_1} \tag{7}$$

where N_0 and N_1 are the number of black (0) and white (1) pixels, respectively.

Quantitative pore size distributions were obtained from high-magnification SEM images (250,000 x). Individual pore areas were measured using the same MATLAB software employed for macrovoid analysis (see example of this analysis in **Fig. S17**). Apparent pore diameters, *d*, were then estimated according to:

$$d = \sqrt{\frac{4A}{\pi}} \tag{8}$$

where *A* is the pore area. These diameters were used to generate pore size distributions and estimate surface porosities and pore diameters (see **Figs. S18-S20)**.

Pure water permeance tests

To measure pure water permeance, a pump delivered MilliQ water from a 4 L feed tank to three dead-end stirred cells (2.5 cm diameter) arranged in series. Prior to testing, water from the feed

tank was passed through a KX CTO/2 carbon-block (5 μm) particle filter (Big Brand Water Filter, Chatsworth, CA) located between the feed tank and pump for 30 min at 300 mL/min, with three commercial PS-20 membranes installed in the dead-end cells. This step removed large particulates (*e.g.*, rust, dust, bacteria) from the water before exposing it to the membranes, following the procedure of Van Wagner *et al.* [46].

Then, cast membranes were punch-cut and placed on top of a porous polypropylene support with negligible hydrodynamic resistance to water transport, and loaded into the dead-end stirred cells. Membranes were pre-pressurized to 15 psig (~1.03 barg) using a back-pressure regulator (Equilibar, Fletcher, NC) for 20 min, after which the pressure was reduced to 10 psig for testing. Permeate masses were collected in beakers placed on electronic balances (Mettler Toledo, Columbus, OH) and recorded automatically over time. At least 500 mL of permeate was collected from each of the three cells, which corresponded to a filtration length of approximately 145 cm (see permeance evolution in **Fig. S21**).

The slope of the mass-time data was used to determine the mass flow rate at intervals corresponding to each 25 mL of collected permeate. These flow rates, divided by the water density, ρ, and normalized by the membrane area, A, were used to calculate the flux, J, according to:

$$J = \frac{\Delta m}{\rho A \Delta t} \tag{9}$$

where Δm is the mass of water permeated through a membrane in a period Δt.

Membrane permeance P was calculated by dividing the flux, J, by the transmembrane pressure Δp.

$$P = \frac{J}{\Delta p} \tag{10}$$

Three replicate measurements were performed for each membrane to determine the mean and 95% confidence interval.

PEG rejection tests

PEG rejection was measured using 1 g/L aqueous PEG solutions (12, 35, 100, and 300 kDa). The solutions were pumped through three dead-end stirred cells (Millipore, Billerica, MA) connected in series. The active area of the membranes was 13.85 cm^2, and the stir speed was held at 250 RPM. The feed pressure was maintained at 6 psig using a back-pressure regulator (Equilibar, Fletcher, NC), and the permeate flux was controlled at 7.25 LMH using a peristaltic pump (Cole-Parmer, Vernon Hills, IL). The low flux and high stir speed minimized concentration polarization. At least 10 mL of the initial permeate was disposed, and the subsequent permeate was collected for HPLC analysis.

Both the feed and all three permeate samples for each PEG molecular weight were analyzed separately using an HPLC system (Thermo Fisher, Waltham, MA) equipped with an SEC column (Acclaim™ SEC-1000) and a charged aerosol detector (Vanquish VF-D20-A). The chromatograms for each molecular weight were combined into a composite chromatogram for the feed and each of the three permeates (see representative chromatograms in **Fig. S22**). This composite chromatogram was divided into 160 slices between 6.25 and 11 min of retention time, and the weight-average molecular weight M_w for each slice was determined using a linear calibration of $\ln(M_w)$ versus retention time, t.

Concentrations in the feed and permeate were estimated from a separate calibration curve relating solution concentration to the integrated peak area of each slice. The apparent rejection for each slice was then calculated as:

$$R = \left(1 - \frac{c_p}{c_f}\right) * 100 \tag{11}$$

where c_p and c_f are the permeate and feed concentrations, respectively. For each membrane, three replicate measurements were used to compute the mean rejection and the 95% confidence interval

To compare block polymer membranes with conventional NIPS membranes, such as PAN, PS-20, PES-100, and PES-300, a separation factor, α, for PEG was calculated from its rejection according to:

$$\alpha = \frac{1}{S} = \frac{1}{1-(R/100)} \tag{12}$$

where S denotes the sieving coefficient. Here, the separation factor, α, corresponds specifically to water and PEG, with water assumed to permeate unhindered (sieving coefficient = 1).

Then, a nonlinear sigmoidal curve was fitted to the PEG rejection profiles to estimate the sharpness parameter, *k*. This curve is given by:

$$R(MW) = R_{min} + \frac{R_{max} - R_{min}}{1+exp\left[-k\left(log(MW)-log(MW_{50})\right)\right]} \tag{13}$$

where R_{min} and R_{max} represent the minimum and maximum rejection values, *k* is the sharpness parameter, and MW_{50} denotes the molecular weight at 50% rejection.

PEG rejection profiles were fitted by minimizing the sum of squared errors between the measured rejections and the model predictions (Eq. 8), using MATLAB's fminsearch function. Initial parameter estimates were obtained directly from the measured values of R_{min}, R_{max}, and MW_{50}, with *k* initially set to 1. Fitting was then performed over PEG molecular weights from 8.5 kDa up to twice the molecular-weight cutoff (MWCO) – defined as the molecular-weight at 90% rejection – with R_{min} and R_{max} treated as free parameters but bounded between 0 % and 100 % (0 % $\leq R_{min} \leq R_{max} \leq$ 100 %).

To enhance fitting accuracy in the 0-90% rejection range, a weighted least-squares approach was employed, applying a uniform weighting factor of 10 to each data point. This factor was chosen after evaluating several values and selecting the one that minimized systematic deviations across the dataset. Finally, each fitted rejection curve — defined by the optimized R_{min}, R_{max}, MW_{50}, and

k – was overlaid on the experimental data to visually assess fit quality (see PEG rejection and pure water permeance for commercial membranes in **Fig. S23** and representative fits in **Figs. S24-S25**).

Results and Discussion

SAN4VP as a block polymer readily accessible by dispersion polymerization

To validate our hypothesis on the effect of the AN comonomer on the strength of isoporous membranes, we examined a series of block polymers with varied AN content in the hydrophobic block (15, 25, and 40 mol%). The S4VP block polymer was synthesized via sequential anionic polymerization – although synthesis via controlled radical polymerization was also feasible – while the SAN4VP block polymers were prepared through a two-step RAFT polymerization. This process consisted of (i) solution polymerization of 4-vinyl pyridine in the presence of a chain transfer agent and (ii) dispersion polymerization of styrene and acrylonitrile in a water/alcohol solvent mixture (see synthetic scheme in **Fig. 1**). Dispersion polymerization is widely used in industry to synthesize high-molecular weight polymers, as it minimizes increases in solution viscosity, reduces excess organic waste, and attains high polymerization rates [47]. The combination of efficiency and sustainability makes this approach particularly attractive for large-scale membrane manufacturing.

The block polymers used in this study are summarized in **Table 1** and labeled SAN_x4VP, where x represents the mol % of AN compared to styrene targeted during the dispersion polymerization. The exception is SAN_04VP, which is labeled S4VP.

All four block polymers had similar number-average molecular weights (112-121 kDa), P4VP contents (24-25 wt.%), and dispersities (1.2-1.5) (see ^{1}H NMR spectra in **Figs. S1-S5**, GPC traces in **Fig. S6**). However, they differed in AN content, which ranged from 0 mol % to 40 mol% in the hydrophobic SAN block. FTIR spectroscopy confirmed this difference, revealing an increase in

the relative intensity of the nitrile peak at 2,237 cm^{-1} (see FTIR spectra in **Fig. S7**, and summary of block polymer properties in **Table 1** and **S1**). GPC also revealed a slightly higher dispersity for the S4VP block polymer – synthesized via anionic polymerization – likely resulting from inhomogeneous mixing and suboptimal temperature control during the early stages of the 4VP polymerization.

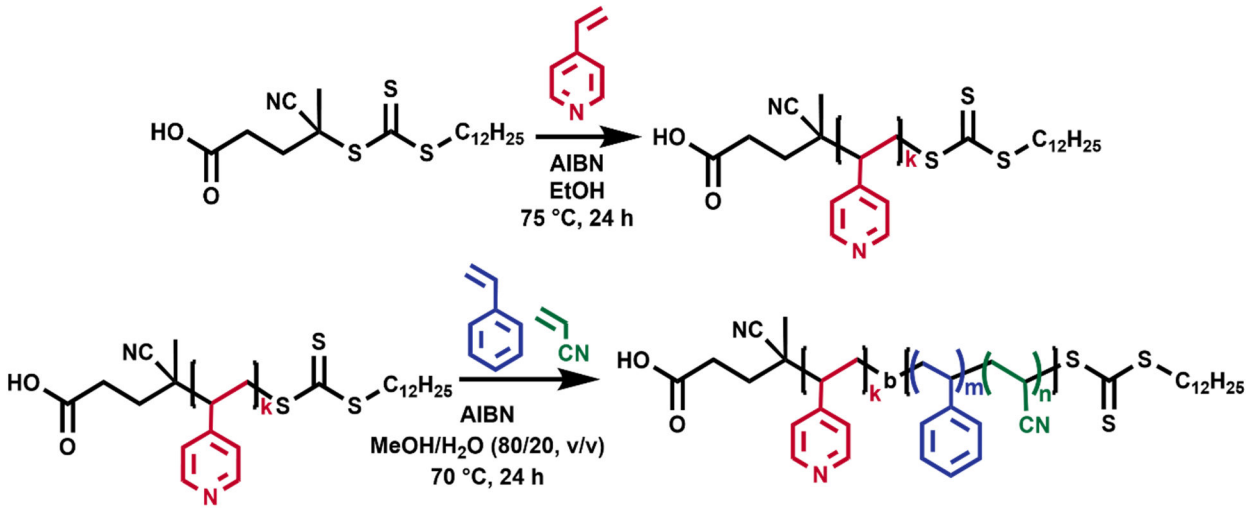

Figure 1. Synthesis of SAN4VP block polymers through two-step RAFT polymerization.

Table 1. Molecular weight, M_n, dispersity, $Đ$, and composition of SAN_x4VP block polymers.

Polymer	Overall M_n* (kg/mol)	Đ	P4VP content (wt.%)	AN content in hydrophobic block (mol%)
S4VP[a]	112	1.5	24	0
$SAN_{15}4VP$[b]	118	1.4	25	15
$SAN_{25}4VP$[b]	118	1.2	25	25
$SAN_{40}4VP$[b]	121	1.2	24	40

[a] synthesized by living, sequential anionic polymerization

[b]synthesized by two-step RAFT polymerization

*calculated from ^{1}H NMR spectra

AN strengthens and toughens styrenic block polymers

The main purpose of incorporating AN into the hydrophobic styrene block was to enhance the mechanical properties of block polymer-based UF membranes. We first examined this improvement in block polymer films cast from 4 wt.% polymer solutions in chloroform, which retained less than 2.5 wt.% residual solvent as determined from mass loss above the glass transition temperature of P4VP, $T_g \approx 140$ °C (see TGA thermograms in **Fig. S8** and DSC traces in **Fig. S9**). Under tension, all dense polymers exhibited a similar Young's modulus, $E \approx 2$ GPa. However, their tensile strength increased with the AN fraction in the hydrophobic block (see representative stress-stretch curves in **Fig. 2**). For instance, S4VP had a tensile strength, σ_f, of 21.6 ± 2.7 MPa, whereas $SAN_{40}4VP$ exhibited nearly double that value at 47 ± 2.4 MPa (see tensile strengths in **Fig. 3a**).

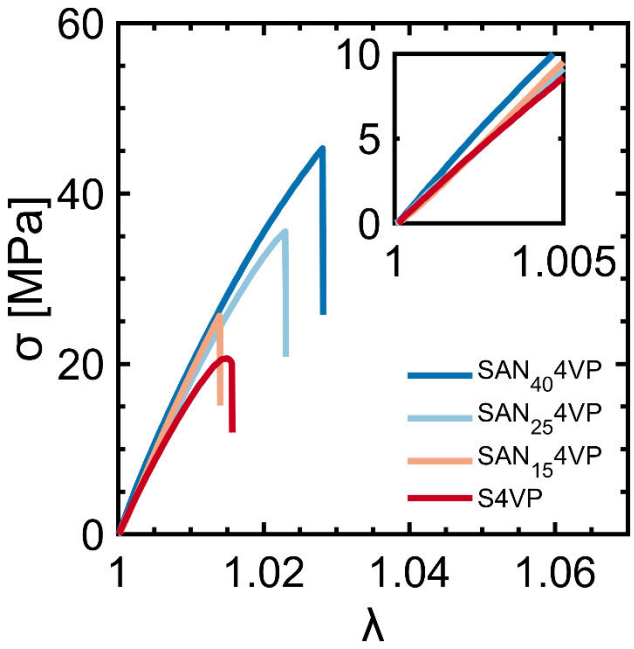

Figure 2. Representative stress-stretch curves of dense SAN4VP block polymers. The tensile strength increased with AN content, while the fracture mode remained brittle. Inset highlights that the Young's modulus was approximately constant.

The stress-stretch curves of these polymers revealed that adding AN to the styrenic block increased the tensile strength without altering the fracture behavior. The SAN4VP block polymers remained brittle, breaking suddenly at relatively low stretch ratios of $\lambda_c \approx 1.02–1.03$, which is consistent with previous studies comparing the tensile properties of PS and SAN. For example, Yokouchi *et al.* reported that the tensile strength of SAN with 40 mol% AN content consistently exceeded that of PS across a wide range of applied strain rates, while showing no significant change in the stretch at break [10].

Such an increase in tensile strength was also evident in the fracture toughness, K_c, as measured by single-edge notch tensile tests (SENT). K_c, also known as the critical stress-intensity factor, quantifies the local stress intensity around the crack tip, beyond which the block polymers fracture. The S4VP copolymer, which contains no AN, exhibited the lowest toughness, $K_c = 0.85 \pm 0.08$ MPa.m$^{1/2}$, similar to previously reported values for homopolymer PS, $K_c = 1.1$ MPa.m$^{1/2}$ [42]. However, as the AN content in the hydrophobic block increased to 40 mol%, the block polymer exhibited a nearly threefold enhancement in toughness, reaching $K_c = 2.7 \pm 0.37$ MPa.m$^{1/2}$ (see representative stress-stretch curves for pre-notched specimens in **Fig. S11** and fracture toughness in **Fig. 3b**).

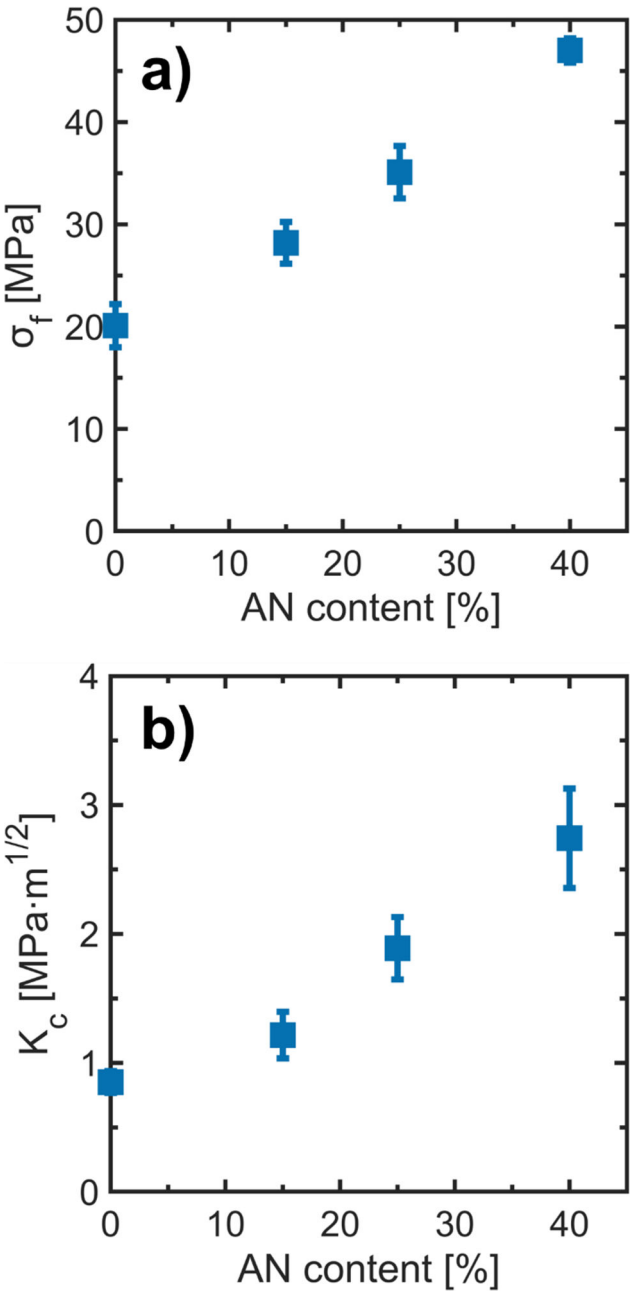

Figure 3. (a) Tensile strength and (b) stress intensity factor of block polymers revealed enhanced mechanical properties with the incorporation of AN into the styrenic block.

Fragility tests on the block polymers offered insights into the toughening mechanism. These tests enable direct observation of the fracture process by supporting thin films on a centimeter-scale copper grid and deforming the grid – and its numerous grid squares – in tension [43,48,49]. Further,

they offer a quantitative measure of the fraction of grid squares, *p*, that develop crazes, SDZs, and cracks at a given strain, providing valuable information about the failure modes.

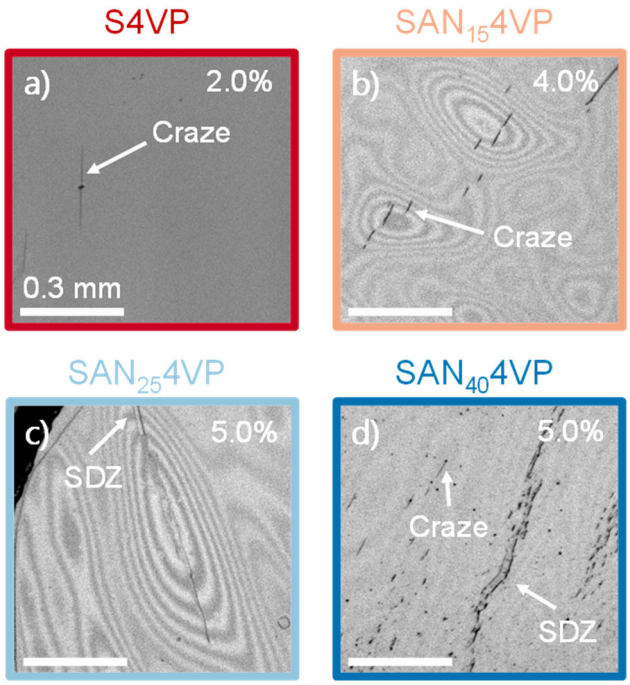

Figure 4. Representative optical microscope images of dense block polymer films. Crazes were observed in S4VP and $SAN_{15}4VP$, while $SAN_{25}4VP$ and $SAN_{40}4VP$ exhibited a mixture of crazes and SDZs. Top right of each image approximately corresponds to the strain at which 50% of the grid squares underwent plastic deformation. All scale bars represent 0.3 mm.

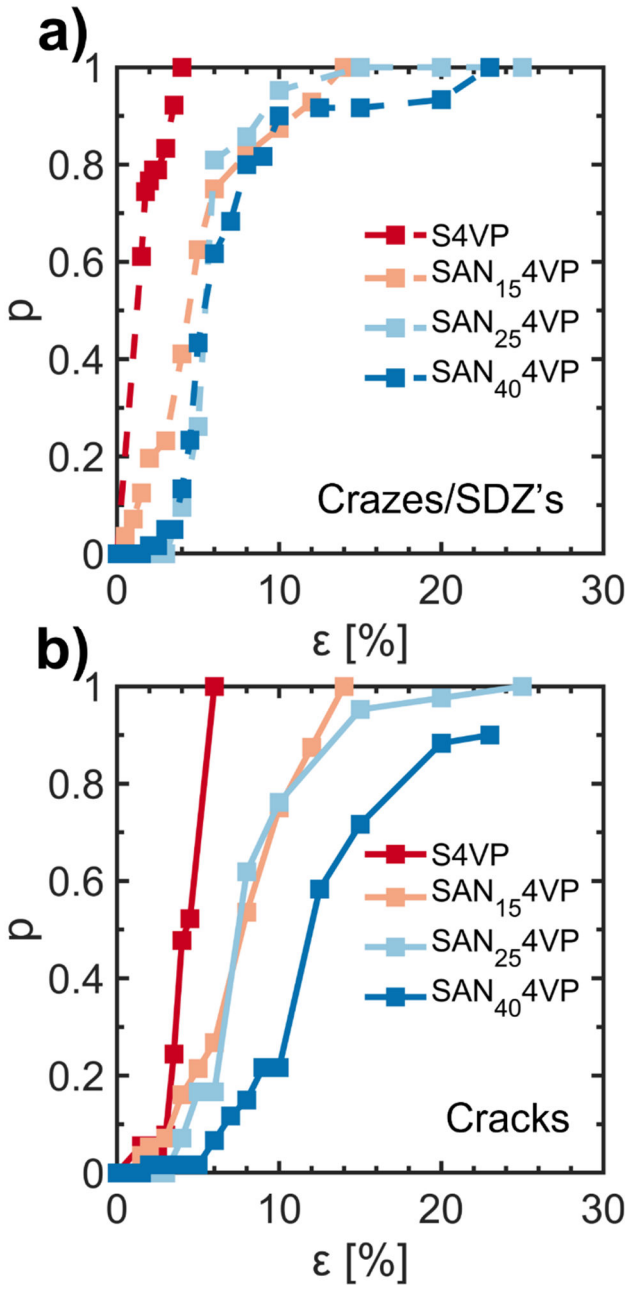

Figure 5. Fraction of grid squares, *p*, that formed (a) crazes and/or SDZs and (b) cracks showed that higher strains were required to initiate fracture in SAN4VP polymers.

Specifically, fragility tests revealed that incorporating AN into the styrenic block both shifts the onset of plastic deformation to higher strains and delays fracture (**Figs. 4-5**). As the AN content

increased from 0 to 40 mol%, the strain at which 50% of the grid squares developed crazes or SDZs rose from ≈ 1.2% to ≈ 5.4%, while the strain at which 50% of the grid squares evolved cracks increased from ≈ 4.3% to ≈ 12% (see strain corresponding to $p = 0.5$ in red and dark blue curves in **Figs. 5a-5b**). These results demonstrate the enhanced fracture resistance of AN-rich block polymers.

Together with the optical micrographs (**Fig. 4**) – which illustrate a transition from crazing-dominated failure at low AN content to an energy-absorbing combination of crazes and SDZs at higher AN – these observations show that AN both strengthens and toughens the block polymers. The improvement likely stems from increased chain entanglements and stronger intermolecular nitrile-nitrile interactions, which promote a more dissipative failure mechanism by distributing stress and delaying crack propagation. This mechanistic picture aligns with earlier observations by Donald and Kramer in SAN statistical copolymers [33].

Relative to S4VP, SAN4VP block polymers offered membranes with similar pore size distributions at the surface, but different porosities within the bulk

Having established that AN enhances the mechanical strength and toughness of styrenic block polymers, we then focused on casting UF membranes by SNIPS. To this end, we identified an initial set of casting conditions from Radjabian *et al.* [50] and optimized them to produce relatively isoporous membranes. The final optimized casting conditions involved using 11 wt.% block polymer solutions in a 65/28/7 wt.% blend of DOX/THF/DMF, a 25-second dry step time, and water as a non-solvent (see SEM images of membranes cast under alternative conditions in **Figs. S12-13**).

Notably, the incorporation of AN altered the appearance of the casting solutions from optically transparent to opaque. This observation suggests that AN influences the solution self-assembly of

styrenic block polymers by promoting the formation of micellar aggregates large enough to scatter light. Grazing-Incidence Small-Angle X-Ray Scattering (GISAXS) profiles of blade-coated block polymers solutions supports this hypothesis, revealing a higher-order peak at $q/q^* = \sqrt{3}$ characteristic of hexagonally packed, ordered micellar structures before immersion in the non-solvent (see scattering profiles in **Fig. S10**).

Despite these changes in solution structure, the cast membranes exhibited similar surface pores and pore size distributions, irrespective of the AN content (see representative SEM images in **Fig. 6**). Quantitative image analysis confirmed this observation, revealing average pore diameters ranging from 21.2 to 24.3 nm and standard deviations around 4.9 nm (see schematic workflow for pore size image analysis in **Fig. S17**, pore size distributions in **Fig. S18**, surface porosities in **Fig. S19**, and pore sizes in **Fig. S20**).

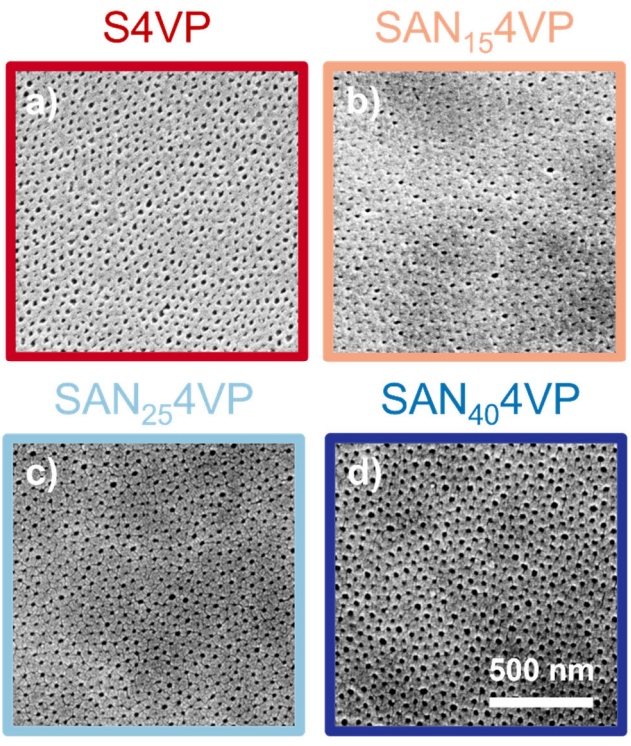

Figure 6. SEM images of membrane surfaces revealed similar pores and pore size distributions. Membranes were cast from 11 wt.% solutions in 65/28/7 wt.% DOX/THF/DMF using a 25 s dry step time and water as a non-solvent. a) S4VP, b) $SAN_{15}4VP$, c) $SAN_{25}4VP$, and d) $SAN_{40}4VP$.

The incorporation of AN, however, led to the formation of large, bulbous macrovoids within the membrane substructure (see **Fig. 7**). In the absence of AN, the substructure was microporous, with a maximum pore size of about 1 μm. By contrast, in the presence of AN, the substructure featured large macrovoids with major axis length of 20-40 μm. Quantification of substructure macroporosity, D_m, using the procedure of Bridge *et al.* [45] (see Eq. 2) revealed that all three SAN4VP membranes had $D_m \approx 0.5$ whereas S4VP had $D_m \approx 0$.

The mechanism responsible for macrovoid formation remains a topic of active investigation [51–53] and is widely believed to be associated with instantaneous polymer demixing upon immersion in a nonsolvent [54]. Within this framework, incorporating hydrophilic AN into the styrenic block may have brought the polymer solutions closer to the binodal curve, increasing solution turbidity and promoting the formation of larger macrovoids. This hypothesis is consistent with our current observations, but further experiments are required to validate it. Still, the differences in macroporosity between S4VP and SAN4VP are important to consider when evaluating the mechanical and transport properties, as they directly affect the ability of block polymer membranes to bear mechanical loads and allow water flow.

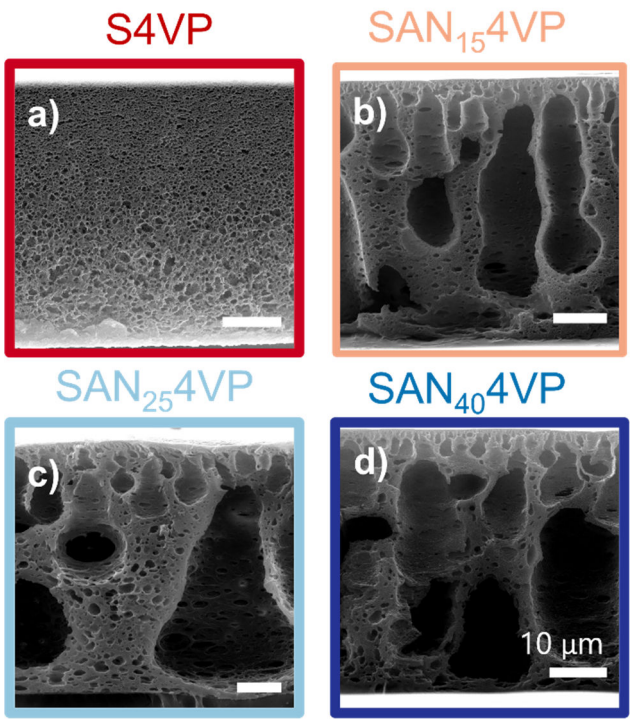

Figure 7. Cross-sectional SEM images of block polymer membranes showed a marked increase in substructure porosity with the incorporation of AN. All membranes were cast from 11 wt.% solutions in 65/28/7 wt.% DOX/THF/DMF using a 25 s dry-step time and water as a nonsolvent. a) S4VP, b) $SAN_{15}4VP$, c) $SAN_{25}4VP$, d) $SAN_{40}4VP$.

AN enhanced the mechanical properties of porous block polymer membranes

To assess the mechanical properties of the asymmetric membranes, we conducted tensile tests on dogbone-shaped specimens immersed in water (see representative stress-stretch curves in **Fig. 8a**). Membranes with low AN content, S4VP and $SAN_{15}4VP$, were softer than those with high AN content, $SAN_{25}4VP$ and $SAN_{40}4VP$, exhibiting elastic moduli E_{S4VP} = 76 ± 18 MPa and E_{SAN15} = 107 ± 5 MPa compared to E_{SAN25} = 202 ± 5 MPa and E_{SAN40} = 176 ± 26 MPa. In addition, these low-AN membranes were weaker, with tensile strengths of $\sigma_{f,S4VP} \approx \sigma_{f,SAN15} \approx 1.4 \pm 0.1$ MPa relative to $\sigma_{f,SAN25} \approx 2.3 \pm 0.3$ and $\sigma_{f,SAN40} \approx 4.2 \pm 1.5$ MPa.

To rationalize these observations, we estimated the stress carried by the polymer (*i.e.*, solid) phase within the membrane, $\sigma^{Polymer}$, by renormalizing the nominal stress, σ, using the substructure macroporosity, D_m, according to:

$$\sigma^{Polymer} = \frac{F}{A_{cross}(1-D_m)} = \frac{\sigma}{1-D_m} \quad (14)$$

Here, F is the tensile force and A_{cross} is the membrane's cross-sectional area in the initial, undeformed state. This normalization, similar to that used in composites [55,56], offered insights into the impact of AN on the mechanical properties (see renormalized stress-stretch curves in **Fig. 8b**). Incorporating AN into the styrenic block enhanced the normalized tensile strength of the porous membranes, in agreement with the behavior observed in the dense polymers (see stress-stretch curves in **Fig. 3**, and onsets of plastic deformation and crack nucleation in **Figs. 4-5**). Thus, membranes manufactured from stronger and tougher block polymers could tolerate larger defects or macrovoids without breaking, highlighting the importance of molecular design for developing advanced materials for emerging separations.

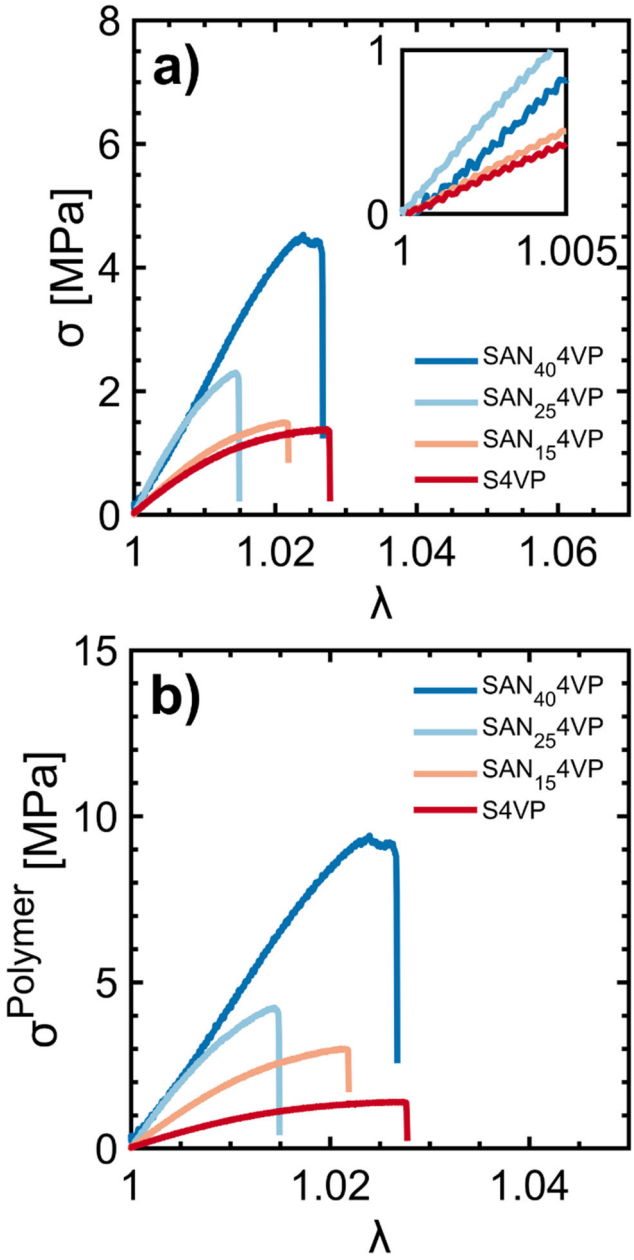

Figure 8. (a) Representative stress-stretch curves of hydrated block polymer membranes. Inset illustrates curves up to a stretch of λ = 1.005, highlighting differences in Young's moduli. (b) Renormalized stress-stretch curves revealed that AN-containing membranes are all stronger than S4VP.

SAN4VP platform highlights opportunities for co-designing of mechanical and transport properties of block polymer membranes

Lastly, to assess the impact of AN content on membrane transport, we conducted PEG rejection and pure water permeance tests on both our block polymer membranes and commercially available NIPS membranes, such as PES-100, PES-300, PS-20, and PAN.

Analysis of the PEG rejection curves revealed a shift toward lower MWCOs – defined at 90% rejection – with increasing AN content (see details of the analysis in the Materials and Methods section and **Fig. S22**). Specifically, the S4VP and SAN_{15}4VP membranes exhibited MWCOs of 157 ± 11 kDa and 189 ± 11 kDa, respectively, while the SAN_{25}4VP and SAN_{40}4VP membranes featured MWCOs of 97 ± 23 kDa and 75 ± 3 kDa – with 95% confidence intervals estimated from three independent measurements (see **Fig. 9a**). In terms of Stokes' diameters, these MWCOs correspond to 26.4 ± 1.0 nm (S4VP), 28.8 ± 0.9 nm (SAN_{15}4VP), 20.2 ± 2.6 nm (SAN_{25}4VP), and 17.6 ± 0.4 nm (SAN_{40}4VP), which closely match the pore sizes measured via SEM and thus suggest that the surface layer provides the primary resistance to PEG transport (see details on the calculations of Stokes' diameters in the SI). Moreover, the fitted steepness parameter, k, increased from $k = 3.4 \pm 0.3$ for S4VP to 4.8 ± 0.6 for SAN_{40}4VP, indicating that adding AN to the structural block enhances the selectivity of the block polymer membranes (see fits in **Fig. S24**).

In pure water permeance tests, membranes with higher MWCOs and broader rejection curves, such as S4VP and SAN_{15}4VP, exhibited initial permeances of 2,100 ± 75 LMH/bar and 2,800 ± 200 LMH/bar, respectively – here, initial refers to measurements after 7 cm of filtration length, and the 95% confidence intervals were estimated from three independent measurements. Such S4VP permeance is notably higher than reported in previous work [15, 57,58], likely due to our lower dope concentration (11 wt.%) and the lower molecular weight of the block polymer (112 kDa). In

contrast, membranes with lower MWCOs and steeper rejection curves, such as SAN_{25}4VP and SAN_{40}4VP, showed permeances of 62 ± 3 LMH/bar and 1,300 ± 300 LMH/bar, respectively (see **Fig. 9b**). These permeances decreased by 24% (S4VP), 31% (SAN_{15}4VP), 34% (SAN_{25}4VP), and 45% (SAN_{40}4VP) over a filtration length of 150 cm (*i.e.*, or long times), likely due to fouling or flow-induced changes to the membrane structure (see **Fig. S21**). Overall, these results align with the well-known permeability-selectivity trade-off in UF membranes [59-61], typically attributed to differences in microstructural features such as pore size distribution, surface porosity, pore tortuosity, and selective layer thickness. Further, they highlight the need to investigate fouling resistance of block polymer membranes and incorporate this dimension into novel molecular designs.

Because all four membranes share similar pore size distributions and surface porosities, the observed differences in water permeance and PEG rejection likely stem from variations in selective layer thickness or tortuosity – both challenging to measure with conventional methods. SEM images of the membranes' bottom surfaces– the sides initially in contact with the glass substrates during phase inversion - partially support this hypothesis, qualitatively revealing a markedly lower bottom-surface porosity in SAN_{25}4VP: the membrane with the lowest permeance (see **Fig. S14**). However, high-magnification cross-sectional SEM images do not allow stronger conclusions, as they lack a clear boundary between the selective layer and therefore cannot be used for comparing the water permeance with well-established pore flow models (see **Fig. S15**).

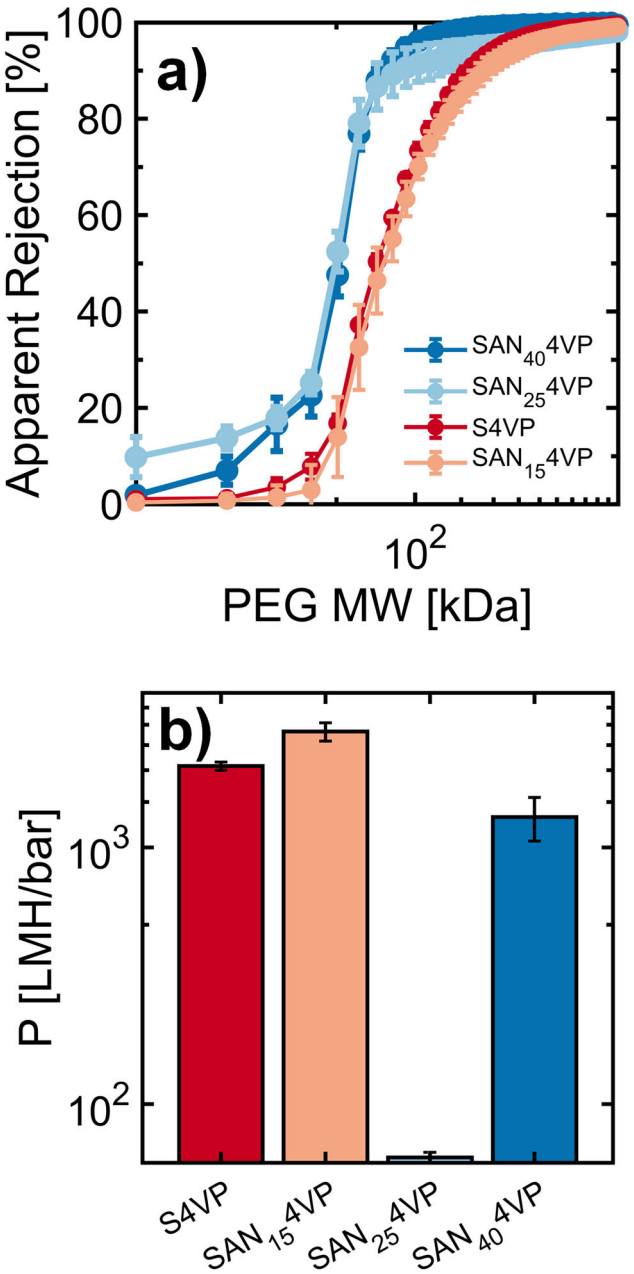

Figure 9. (a) Average apparent PEG rejection profiles for block polymer membranes with varying AN content, showing a shift to lower MWCO at higher AN. (b) Average pure water permeance for the same membranes, showing reduced permeance with increasing AN. Error bars indicate 95% confidence intervals

Relative to block polymer membranes, commercial NIPS membranes spanned a similar range of MWCOs and steepness parameters. For example, PS-20 exhibited MWCO = 53 ± 7 kDa and k = 2.2 ± 0.3, whereas PAN showed MWCO = 94 ± 3 kDa and k = 7.3 ± 0.1. However, with the exception of $SAN_{25}4VP$, their pure water permeances were lower – ranging from 14 ± 1 LMH/bar for PAN to 731 ± 12 LMH/bar for PS-20 (see PEG rejection curves and pure water permeances for commercial NIPS membranes in **Fig. S23**, and fits in **Fig. S25**). Therefore, these commercial NIPS membranes follow a similar permeability-selectivity trade-off – quantified by the PEG separation factor, α, at a given molecular weight – as the block polymer membranes; but occupy the low-permeance, high-separation factor region of the upper bound plot rather than the high-permeance, low-separation factor end (see separation factor at 70 kDa in **Fig. 10** and at 20 kDa and 100 kDa in **Fig. S26**).

Collectively, these results highlight two important points. First, block polymer self-assembly may lead to membranes with narrowly distributed surface pores, but these pores alone do not necessarily dictate the separation performance. Subtle changes in selective layer thickness and substructure porosity may also play an important role. Second, block polymer membranes may be isoporous, but their permeability-selectivity trade-off is similar to that of commercial NIPS membranes within the pore size range studied. Their higher permeances and lower separation factors simply reflect their position in a different region of the upper-bound plot.

In sum, this work highlights the complexity of co-designing the mechanical and transport properties in UF membranes. Incorporating AN into the hydrophobic block improves the strength and toughness relative to S4VP but also affects the water permeance, MWCO, and PEG separation factor (see **Table 2**). Relative to commercial NIPS membranes, these block polymer membranes exhibit higher water permeances and lower separation factors but still lie below the same

permeability-selectivity upper bound curve. SAN-based block polymers, hence, represent a promising material platform for future studies aimed at developing strong, permeable, and highly selective phase-inversion membranes, where understanding how to optimize selective layer structure and thickness will be key for achieving both high flux and sharp separation.

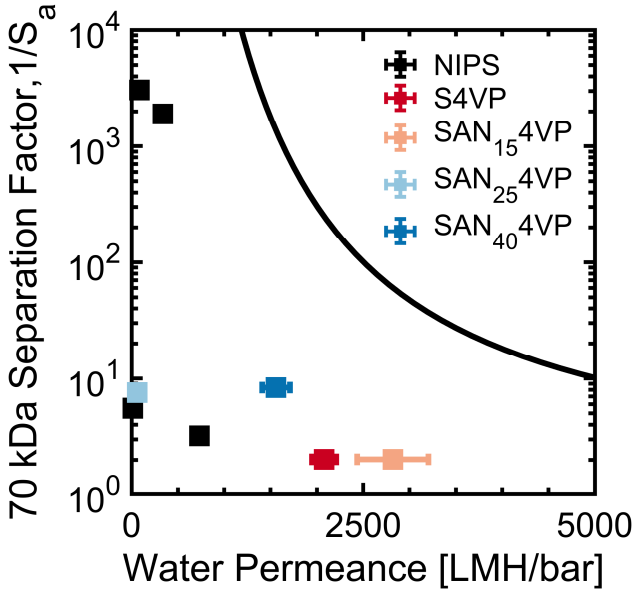

Figure 10. Separation factor at 70 kDa versus initial pure water permeance for block polymer and commercial NIPS membranes, illustrating the permeability-selectivity tradeoff. The solid black line is the predicted upper bound for 70 kDa PEG (Stokes radius = 8.36 nm) calculated using a coefficient of variation of 0.2 and a porosity-thickness ratio of 1 μm^{-1}, following Mehta *et al.* [60].

Table 2. Summary of key mechanical and transport properties of the block polymer membranes. Uncertainties represent standard error of the mean (68% confidence interval).

Membrane	Pure water permeance (LMH/bar)	MWCO (kDa)	Tensile strength (MPa)
S4VP	2,100 ± 75	160 ± 4	1.44 ± 0.10
$SAN_{15}4VP$	2,800 ± 200	186 ± 10	1.42 ± 0.15
$SAN_{25}4VP$	62 ± 3	99 ± 23	2.31 ± 0.25

$SAN_{40}4VP$	1,300 ± 300	77 ± 3	4.17 ± 1.32

Conclusions

As membranes find use in increasingly complex separations, co-designing their mechanical and transport properties becomes important for scalable manufacturing. Here, we synthesized a series of styrenic block polymers via RAFT polymerization, incorporating acrylonitrile into the hydrophobic block to enhance mechanical strength and toughness. We cast these block polymers from a DOX/THF/DMF solvent blend and immersed the films in a water nonsolvent, obtaining membranes with surface pores comparable to state-of-the-art poly(styrene-*b*-4-vinyl pyridine) membranes, but with a markedly more porous substructure.

The incorporation of acrylonitrile into the styrenic block improved the mechanical strength and toughness of the membranes by facilitating chain entanglements, strengthening interchain interactions, and changing the failure mode from pure crazing to a combination of crazing and shear deformation. However, this enhancement in mechanical properties had complex effects on separation performance, reducing pure water permeance while increasing the PEG separation factor. Likely, acrylonitrile induced subtle, hard-to-detect changes in the selective layer thickness or substructure that increased the hydrodynamic resistance to water flow.

Despite this intricate balance between mechanical and transport properties, the block polymer membranes featured significantly higher pure water permeances than conventional NIPS membranes, highlighting their potential for UF. However, these results also reveal an important challenge: current block polymer designs and phase inversion methods afford limited control over membrane substructure. Addressing this limitation is the focus of ongoing work and essential for optimizing separation performance and enabling scalable manufacturing. For example, Zhang *et al.* incorporated a dip-coating step into the SNIPS process to coat a thin – 200 nm to 2,000 nm -

block polymer selective layer onto a hollow fiber support [62]. Their work, like ours, underscores the need to combine a well-defined substructure with a self-assembled selective layer to manufacture high performance UF membranes.

Author Contributions

Conceptualization (A.N.M., B.D.F., and G.E.S), data curation (A.N.M., N.P.W., L.K., M.R.L., and A.J.A.), data analysis (A.N.M., N.P.W., L.K., and M.R.L.), funding acquisition (G.M.S., N.A.L., B.D.F., and G.E.S.), investigation (A.N.M., N.P.W., L.K., M.R.L., B.D.F., and G.E.S.), resources (G.M.S., N.A.L., B.D.F., and G.E.S.), supervision (G.M.S., N.A.L., B.D.F., and G.E.S.), validation (A.N.M., N.P.W., L.K., M.R.L., G.M.S., N.A.L., B.D.F., and G.E.S.), visualization (A.N.M., N.P.W., L.K., M.R.L., and G.E.S.), writing – original draft (A.N.M.), writing – review and editing (A.N.M., N.P.W., L.K., M.R.L, G.M.S., N.A.L., B.D.F., and G.E.S.).

Supporting Information

Molecular characterization of polymers (^{1}H NMR and GPC), thermal characterization of polymers (TGA and DSC), solution self-assembly of block polymers (GISAXS), single-edge notch fracture tests (stress-stretch curves), SEM images, porosity quantification via image analysis, characterization of transport properties (HPLC chromatograms and rejection curves).

Author Information

Corresponding Author

Gabriel E. Sanoja – Department of Chemical Engineering, University of Texas at Austin, Austin, Texas 78712, United States; Orcid ID: https://orcid.org/0000-0001-5477-2346; E-mail: gesanoja@che.utexas.edu

Authors

Adam N. Mann – Department of Chemical Engineering, University of Texas at Austin, Austin, Texas 78712, United States; https://orcid.org/0009-0004-7533-3819

Noah P. Wamble – Department of Chemical Engineering, University of Texas at Austin, Austin, Texas 78712, United States; https://orcid.org/0000-0003-0769-727X

Louise Kuehster – Department of Chemical Engineering, University of Texas at Austin, Austin, Texas 78712, United States; https://orcid.org/0000-0002-0730-204X

Matthew R. Landsman – Advanced Light Source, Lawrence Berkeley National Laboratory, Berkeley, California 94720, United States; https://orcid.org/0000-0002-4803-1645

Gregory M. Su – Advanced Light Source and Materials Science Division, Lawrence Berkeley National Laboratory, Berkeley, California 94720, United States; https://orcid.org/0000-0001-7495-8041

Nathaniel A. Lynd – Department of Chemical Engineering, University of Texas at Austin, Austin, Texas 78712, United States; https://orcid.org/0000-0003-3010-5068

Benny D. Freeman – Department of Chemical Engineering, University of Texas at Austin, Austin, Texas 78712, United States; https://orcid.org/0000-0003-2779-7788

Notes

A.N.M., BD.F., and G.E.S. declare filing of a provisional patent application to the United States Patent and Trademark Office, entitled "SAN-Based Block Copolymers for Membranes" (US 63/800,715). *Data and Materials Availability.* All data needed to evaluate the conclusions are present in the paper and/or Supporting Information, as well as in the Texas Data Repository at https://doi.org/10.18738/T8/FKY5WP.

Acknowledgments

This work was supported as part of the Center for Materials for Water and Energy Systems (M-WET), an Energy Frontier Research Center funded by the U.S. Department of Energy, Office of Science, Basic Energy Sciences under Award #DE-SC0019272. This research used resources of the National Synchrotron Light Source II (beamline 12-ID), a U.S. DOE Office of Science User Facility operated by Brookhaven National Laboratory under contract #DE-SC0012704. The development of the custom-built strain frame was supported by the donors of the ACS Petroleum Research Fund under Doctoral New Investigator Grant 68753-DNI7. The authors also wish to thank Rachel A. Segalman, Costantino Creton, Alfred J. Crosby, Konane Bay, and Michael Chabinyc for their insightful discussions on the copper grid technique, and Kris Gleason for support in conducting the long-term permeance experiments

References

[1] J.C.D. Fell, Reverse Osmosis, in: R.D. Noble, S.A. Stern (Eds.), Membr. Sep. Technol. Princ. Appl., 1st ed., Elsevier, Amsterdam, 1995: p. 718. ISBN: 978-0-444-81633-7.

[2] L.J. Zeman, A.L. Zydney, Microfiltration and Ultrafiltration: Principles and Applications, 1st ed., Marcel Dekker, Inc., New York, 1996: pp. 51-121. https://doi.org/10.1201/9780203747223.

[3] R.W. Baker, Membrane Technology and Applications, 2nd ed., John Wiley & Sons, Inc, Chichester,West Sussex, 2004: pp. 96-109. https://doi.org/10.1002/0470020393.

[4] M. Mulder, Basic Principles of Membrane Technology, 2nd ed., Springer Dordrecht, 1996: pp.71-156. https://doi.org/10.1007/978-94-009-1766-8.

[5] M. Cheryan, Ultrafiltration and Microfiltration Handbook, 2nd ed., CRC Press, Boca Raton, Florida, 1998. pp. 39-41. https://doi.org/10.1201/9781482278743.

[6] M.C. Porter, Microfiltration, in: P.M. Bungay, H.K. Lonsdale, M.N. de Pinho (Eds.), Synth. Membr. Sci. Eng. Appl., Reidel Publishing Company, Boston, 1986: pp. 225–247. https://doi.org/10.1007/978-94-009-4712-2_9.

[7] R. Singh, Introduction to Membrane Technology, in: R. Singh (Ed.), Membr. Technol. Eng. Water Purif., 2nd ed., Butterworth-Heinemann, 2015: pp. 1–80. https://doi.org/10.1016/B978-0-444-63362-0.00001-X.

[8] S. Jamal El-Hibri, M. Weinberg, Polysulfones, Encycl. Polym. Sci. Technol. (2001). p. 1. https://doi.org/10.1002/0471440264.pst291.

[9] H. Sun, J.E. Mark, Preparation, Characterization, and Mechanical Properties of Some

Microcellular Polysulfone Foams, J. Appl. Polym. Sci. 86 (2002) 1692–1701. https://doi.org/10.1002/app.11070.

[10] M. Yokouchi, S. Seto, Y. Kobayashi, Comparison of Polystyrene, Poly(styrene/ Acrylonitrile), High-Impact Polystyrene, and Poly(acrylonitrile/Butadiene/Styrene) with Respect to Tensile and Impact Properties, J. Appl. Polym. Sci. 28 (1983) 2209–2216. https://doi.org/10.1002/app.1983.070280707.

[11] L.J. Gibson, M.F. Ashby, The Mechanics of Foams : Basic Results, in: Cell. Solids Struct. Prop., 2nd ed., Cambridge University Press, 1997: pp. 175–234. https://doi.org/10.1017/CBO9781139878326.007.

[12] V. Abetz, Isoporous Block Copolymer Membranes, Macromol. Rapid Commun. 36 (2015) 10–22. https://doi.org/10.1002/marc.201400556.

[13] C. Lang, M. Kumar, R.J. Hickey, Current Status and Future Directions of Self-Assembled Block Copolymer Membranes for Molecular Separations, Soft Matter 17 (2021) 10405–10415. https://doi.org/10.1039/d1sm01368h.

[14] J. Hahn, V. Filiz, S. Rangou, B. Lademann, K. Buhr, J.I. Clodt, A. Jung, C. Abetz, V. Abetz, PtBS-b-P4VP and PTMSS-b-P4VP Isoporous Integral-Asymmetric Membranes with High Thermal and Chemical Stability, Macromol. Materials Eng. 298 (2013) 1315–1321. https://doi.org/10.1002/mame.201300012.

[15] R. Shevate, M. Karunakaran, M. Kumar, K.V. Peinemann, Polyanionic pH-responsive Polystyrene-b-poly(4-vinyl pyridine-N-oxide) Isoporous Membranes, J. Memb. Sci. 501 (2016) 161–168. https://doi.org/10.1016/j.memsci.2015.11.038.

[16] T. Wu, Z. Wang, F. Yin, W. Wang, Z. Yi, Isoporous Membranes by the Symmetric Triblock Copolymer: A Strategy to Improve the Mechanical Strength without Sharply Changing the Pore Size and Permselectivity, ACS Appl. Mater. Interfaces 16 (2024) 37073–37086. https://doi.org/10.1021/acsami.4c07113.

[17] E.A. Jackson, Y. Lee, M.A. Hillmyer, ABAC Tetrablock Terpolymers for Tough Nanoporous Filtration Membranes, Macromolecules 46 (2013) 1484–1491. https://dx.doi.org/10.1021/ma302414w.

[18] H.R. Brown, A Molecular Interpretation of the Toughness of Glassy Polymers, Macromolecules 24 (1991) 2752–2756. https://doi.org/10.1021/ma00010a018.

[19] C.S. Henkee, E.J. Kramer, Crazing and Shear Deformation in Crosslinked Polystyrene, J. Polym. Sci. Part B Polym. Phys. 22 (1984) 721–737. https://doi.org/10.1002/pol.1984.180220414.

[20] A.R.C. Baljon, M.O. Robbins, Simulations of Crazing in Polymer Glasses: Effect of Chain Length and Surface Tension, Macromolecules 34 (2001) 4200–4209. https://doi.org/10.1021/ma0012393.

[21] J. Rottler, M.O. Robbins, Growth, Microstructure, and Failure of Crazes in Glassy Polymers, Phys. Rev. E - Stat. Physics, Plasmas, Fluids, Relat. Interdiscip. Top. 68 (2003) 18. https://doi.org/10.1103/PhysRevE.68.011801.

[22] C. Bukowski, T. Zhang, R.A. Riggleman, A.J. Crosby, Load-bearing Entanglements in Polymer Glasses, Sci. Adv. 7 (2021) 1–10. https://www.science.org/doi/10.1126/sciadv.abg9763.

[23] R.P. Kambour, Review of Crazing and Fracture in Thermoplastics., J Polym Sci, Part D, Macromol Rev 7 (1973) 1–154. https://doi.org/10.1002/pol.1973.230070101.

[24] S. Wellinghoff, E. Baer, The Mechanism of Crazing in Polystyrene, J. Macromol. Sci. Part B 11 (1975) 367–387. https://doi.org/10.1080/00222347508018918.

[25] A.S. Argon, M.M. Salama, Growth of Crazes in Glassy Polymers, Philos. Mag. 36 (1977) 1217–1234. https://doi.org/10.1080/14786437708239790.

[26] A.M. Donald, E.J. Kramer, The Mechanism for Craze-Tip Advance in Glassy Polymers, Philos. Mag. A Phys. Condens. Matter, Struct. Defects Mech. Prop. 43 (1981) 857–870. https://doi.org/10.1080/01418618108239496.

[27] E.J. Kramer, Craze Fibril Formation and Breakdown, Polym. Eng. Sci. 24 (1984) 761–769. https://doi.org/10.1002/pen.760241006.

[28] B.D. Lauterwasser, E.J. Kramer, Microscopic Mechanisms and Mechanics of Craze Growth and Fracture, Philos. Mag. A Phys. Condens. Matter, Struct. Defects Mech. Prop. 39 (1979) 469–495. https://doi.org/10.1080/01418617908239285.

[29] N. Walker, R.N. Haward, J.N. Hay, Plastic Fracture in Poly(vinyl chloride), J. Mater. Sci. 14 (1979) 1085–1094. https://doi.org/10.1007/BF00561291.

[30] P.L. Cornes, K. Smith, R.N. Haward, Plastic Fracture, J. Polym. Sci. Polym. Phys. Ed. 15 (1977) 955–967. https://doi.org/10.1002/pol.1977.180150603.

[31] P.B. Bowden, The Yield Behaviour of Glassy Polymers, in: R.N. Haward (Ed.), Phys. Glas. Polym., Springer Dordrecht, 1973: pp. 279–339. https://doi.org/10.1007/978-94-010-2355-9_6.

[32] J.C.. Li, Behavior and Properties of Shear Bands, Polym. Eng. Sci. 24 (1984) 750–760. https://doi.org/10.1002/pen.760241005.

[33] A.M. Donald, E.J. Kramer, The Competition Between Shear Deformation and Crazing in glassy polymers, J. Mater. Sci. 17 (1982) 1871–1879. https://doi.org/10.1007/BF00540402.

[34] L.J. Fetters, D.J. Lohse, T.A. Witten, A. Zirkel, Connection between Polymer Molecular Weight, Density, Chain Dimensions, and Melt Viscoelastic Properties, Macromolecules 27 (1994) 4639–4647. https://doi.org/10.1021/ma00095a001.

[35] L.J. Fetters, D.J. Lohse, W.W. Graessley, Chain Dimensions and Entanglement Spacings in Dense Macromolecular Systems, J. Polym. Sci. Part B Polym. Phys. 37 (1998) 1023–1033. https://doi.org/10.1002/(SICI)1099-0488(19990515)37:10<1023::AID-POLB7>3.0.CO;2-T.

[36] W. Chen, M. Wei, Y. Wang, Advanced Ultrafiltration Membranes by Leveraging Microphase Separation in Macrophase Separation of Amphiphilic Polysulfone Block Copolymers, J. Memb. Sci. 525 (2017) 342–348. https://doi.org/10.1016/j.memsci.2016.12.009.

[37] N. Wang, T. Wang, Y. Hu, Tailoring Membrane Surface Properties and Ultrafiltration Performances via the Self-Assembly of Polyethylene Glycol-block-Polysulfone-block-Polyethylene Glycol Block Copolymer upon Thermal and Solvent Annealing, ACS Appl. Mater. Interfaces 9 (2017) 31018–31030. https://doi.org/10.1021/acsami.7b06997.

[38] D.B.P. John Schiers, Modern Styrenic Polymers: Polystyrenes and Styrenic Copolymers, John Wiley & Sons, Inc, 2003. p. 19. https://doi.org/10.1002/0470867213.

[39] A.M. Donald, E.J. Kramer, Effect of Molecular Entanglements on Craze Microstructure in Glassy Polymers, J. Polym. Sci. Part B Polym. Phys. 20 (1982) 899–909. https://doi.org/10.1002/pol.1982.180200512.

[40] R. Browning, H. Sue, R. Minkwitz, P. Charoensirisomboon, Effects of Acrylonitrile Content and Molecular Weight on the Scratch Behavior of Styrene-Acrylonitrile Random Copolymers, Polym. Eng. Sci. (2011) 2282–2294. https://doi.org/10.1002/pen.22003.

[41] A.M. Saum, Intermolecular Association in Organic Nitriles: the CN dipole-pair bond, J. Polym. Sci. 42 (1960) 57–66. https://doi.org/10.1002/pol.1960.1204213907.

[42] A.J. Kinloch, R.J. Young, Fracture Mechanics, in: Fract. Behav. Polym., Applied Science, London, 1983: pp. 74–106. https://doi.org/10.1017/S0001924000020042.

[43] A.C.M. Yang, E.J. Kramer, C.C. Kuo, S.L. Phoenix, Craze Fibril Stability and Breakdown in Polystyrene, Macromolecules 19 (1986) 2010–2019. https://doi.org/10.1021/ma00161a039.

[44] D. Allan, T. Caswell, S. Campbell, M. Rakitin, Bluesky's Ahead: A Multi-Facility Collaboration for an a la Carte Software Project for Data Acquisition and Management, Synchrotron Radiat. News 32 (2019) 19–22. https://doi.org/10.1080/08940886.2019.1608121.

[45] A.T. Bridge, M.S. Santoso, J.A. Maisano, A. V Hillsley, J.F. Brennecke, B.D. Freeman, Rapid Macrovoid Characterization in Membranes Prepared via Nonsolvent-Induced Phase Separation : A Comparison between 2D and 3D Techniques, J. Memb. Sci. 661 (2022) 120923. https://doi.org/10.1016/j.memsci.2022.120923.

[46] E.M. Van Wagner, A.C. Sagle, M.M. Sharma, B.D. Freeman, Effect of Crossflow Testing Conditions, Including Feed pH and Continuous Feed Filtration, on Commercial Reverse Osmosis Membrane Performance, J. Memb. Sci. 345 (2009) 97–109. https://doi.org/10.1016/j.memsci.2009.08.033.

[47] P.A. Lovell, F.J. Schork, Fundamentals of Emulsion Polymerization, Biomacromolecules 21 (2020) 4396-4441. https://doi.org/10.1021/acs.biomac.0c00769.

[48] E.J. Kramer, L.L. Berger, Fundamental Processes of Craze Growth and Fracture, Adv. Polym. Sci. (1990) 68. https://doi.org/10.1007/BFb0018018.

[49] C.Y. Ryu, J. Ruokolainen, G.H. Fredrickson, E.J. Kramer, S.F. Hahn, Chain Architecture Effects on Deformation and Fracture of Block Copolymers with Unentangled Matrices, Macromolecules 35 (2002) 2157–2166. https://doi.org/10.1021/ma011576r.

[50] M. Radjabian, C. Abetz, B. Fischer, A. Meyer, V. Abetz, Influence of Solvent on the Structure of an Amphiphilic Block Copolymer in Solution and in Formation of an Integral Asymmetric Membrane, ACS Appl. Mater. Interfaces 9 (2017) 31224–31234. https://doi.org/10.1021/acsami.6b15199.

[51] M. Sadrzadeh, S. Bhattacharjee, Rational Design of Phase Inversion Membranes by Tailoring Thermodynamics and Kinetics of Casting Solution using Polymer Additives, J. Memb. Sci. 441 (2013) 31–44. https://doi.org/10.1016/j.memsci.2013.04.009.

[52] D. Wang; A. Venault; J. Lai. Fundamentals of Nonsolvent-Induced Phase Separation. In Hollow Fiber Membranes; Elsevier Inc., 2021. pp. 13-56. https://doi.org/10.1016/B978-0-12-821876-1.00009-3.

[53] G.R. Guillen, G.Z. Ramon, H.P. Kavehpour, R.B. Kaner, E.M. V Hoek, Direct Microscopic Observation of Membrane Formation by Nonsolvent-Induced Phase Separation, J. Memb. Sci. 431 (2013) 212–220. https://doi.org/10.1016/j.memsci.2012.12.031.

[54] C.A. Smolders, A.J. Reuvers, R.M. Boom, I.M. Wienk, Microstructures in Phase-Inversion Membranes. Part 1. Formation of Macrovoids *, J. Memb. Sci. 73 (1992) 259–275. https://doi.org/10.1016/0376-7388(92)80134-6.

[55] P. Millereau, E. Ducrot, J.M. Clough, M.E. Wiseman, H.R. Brown, R.P. Sijbesma, Mechanics of Elastomeric Molecular Composites, Proc. Natl. Acad. Sci. 115 (2018) 9110–9115. https://doi.org/10.1073/pnas.1807750115.

[56] L.J. Gibson, M.F.A. Sh, J.G.S. Schajerj, The Mechanics of Two-Dimensional Cellular Materials, Proc. R. Soc. Lond. A 382 (1982) 25–42. https://doi.org/10.1098/rspa.1982.0087.

[57] S.P. Nunes, R. Sougrat, B. Hooghan, D.H. Anjum, A.R. Behzad, L. Zhao, N. Pradeep, I. Pinnau, U. Vainio, K.V. Peinemann, Ultraporous Films with Uniform Nanochannels by Block Copolymer Micelles Assembly, Macromolecules 43 (2010) 8079–8085. https://doi.org/10.1021/ma101531k.

[58] J.I. Clodt, B. Bajer, K. Buhr, J. Hahn, V. Filiz, V. Abetz, Performance Study of Isoporous Membranes with Tailored Pore Sizes, J. Memb. Sci. 495 (2015) 334–340. https://doi.org/10.1016/j.memsci.2015.07.041.

[59] S. Kasemset, L. Wang, Z. He, D.J. Miller, A. Kirschner, B.D. Freeman, M.M. Sharma, Influence of Polydopamine Deposition Conditions on Hydraulic Permeability, Sieving Coefficients, Pore Size and Pore Size Distribution for a Polysulfone Ultrafiltration Membrane, J. Memb. Sci. 522 (2017) 100–115.

https://doi.org/10.1016/j.memsci.2016.07.016.

[60] A. Mehta, A.L. Zydney, Permeability and Selectivity Analysis for Ultrafiltration Membranes, J. Memb. Sci. 249 (2005) 245–249. https://doi.org/10.1016/j.memsci.2004.09.040.

[61] Y. Chen, S. Kim, Y. Cohen, Tuning the Hydraulic Permeability and Molecular Weight Cutoff (MWCO) of Surface Nano-structured Ultrafiltration Membranes, J. Memb. Sci. 629 (2021). https://doi.org/10.1016/j.memsci.2021.119180.

[62] Y. Zhang, R.A. Mulvenna, B.W. Boudouris, W.A. Phillip, Nanomanufacturing of High-Performance Hollow Fiber Nanofiltration Membranes by Coating Uniform Block Polymer Films from Solution, J. Mater. Chem. A 5 (2017) 3358–3370. https://doi.org/10.1039/C6TA09287J.